Published by IOP Publishing for Sissa Medialab

Received: *March 28, 2024*
Accepted: *October 11, 2024*
Published: *December 3, 2024*

An integrated flux-symmetric spectrometer-magnet system for the SND@LHC experiment upgrade

The SND@LHC collaboration

E-mail: loschiavo@unisannio.it, aquercia@unina.it, valentino.scalera@uniparthenope.it

Abstract: The proposed upgrade of the SND@LHC experiment for the High Luminosity phase of the LHC (HL-LHC) will strongly benefit from the presence of a magnetized region, allowing for muon momentum and charge measurement. In this paper we describe an iron core magnet system that is partly integrated with the calorimeter and that is designed to respect the strict constraints from the available space in the experimental cavern, power consumption, and field requirements.

Semi-analytical tools are introduced to explore the parameter space, in order to define the primary design options. A full 3-D analysis is then performed in order to validate the optimal choice, and to propose a conceptual design, including sizing of the components, detector performances and stray fields. Several technical options are also discussed, anticipating the design phase.

Keywords: Muon spectrometers; Particle identification methods

https://doi.org/10.1088/1748-0221/19/12/P12002

2024 JINST 19 P12002

Contents

1 Introduction 1

2 The experimental context 1
  2.1 Physics goals and requirements 2
  2.2 Operational and assembly constraints, and CERN standards 4

3 Electromagnetic design and optimization 5
  3.1 Detector performance and geometrical requirements 5
  3.2 Design optimisation 7
  3.3 3-D electromagnetic analysis 11

4 Complementary design aspects and cost estimate 18
  4.1 Power converters 18
  4.2 Coil cooling 19
  4.3 Magnet assembly aspects 19
  4.4 Cost estimate 19

5 Conclusions 20

The SND@LHC collaboration 23

2024 JINST 19 P12002

1 Introduction

The proposed upgrade of the SND@LHC experiment [1, 2] for the High-Luminosity phase of the LHC (HL-LHC) will inherit the current modular structure based on the synergy between a neutrino target region, where the vertex of neutrino interactions are reconstructed, and a hadronic calorimeter (HCAL) together with a muon identification system. Adding a magnetic field over the HCAL and the muon system will allow for momentum and charge measurement of muons.

The magnetization of the HCAL/muon identification system will improve the neutrino energy measurement and will allow discriminating between neutrinos and antineutrinos when muons are produced in the final state. The magnet system will consist of two parts. The HCAL, consisting of 21 scintillating bar planes interleaved by 22 magnetised iron slabs for a total of 10 interaction lengths (λ), will be equipped with the Hadronic Calorimeter Magnet (HCM). The muon identification system will consist of an iron core magnet, referred to as Muon System Magnet (MSM), instrumented with three tracking stations based on drift tubes. The overall layout of the proposed magnetized SND detector is shown in figure 1, with dimensions included.

2 The experimental context

The new magnetized detector is foreseen to be placed in the same area where the SND@LHC detector is currently located, i.e. in the TI18 tunnel at about 480 m from the ATLAS [3] proton-proton interaction point (IP1).

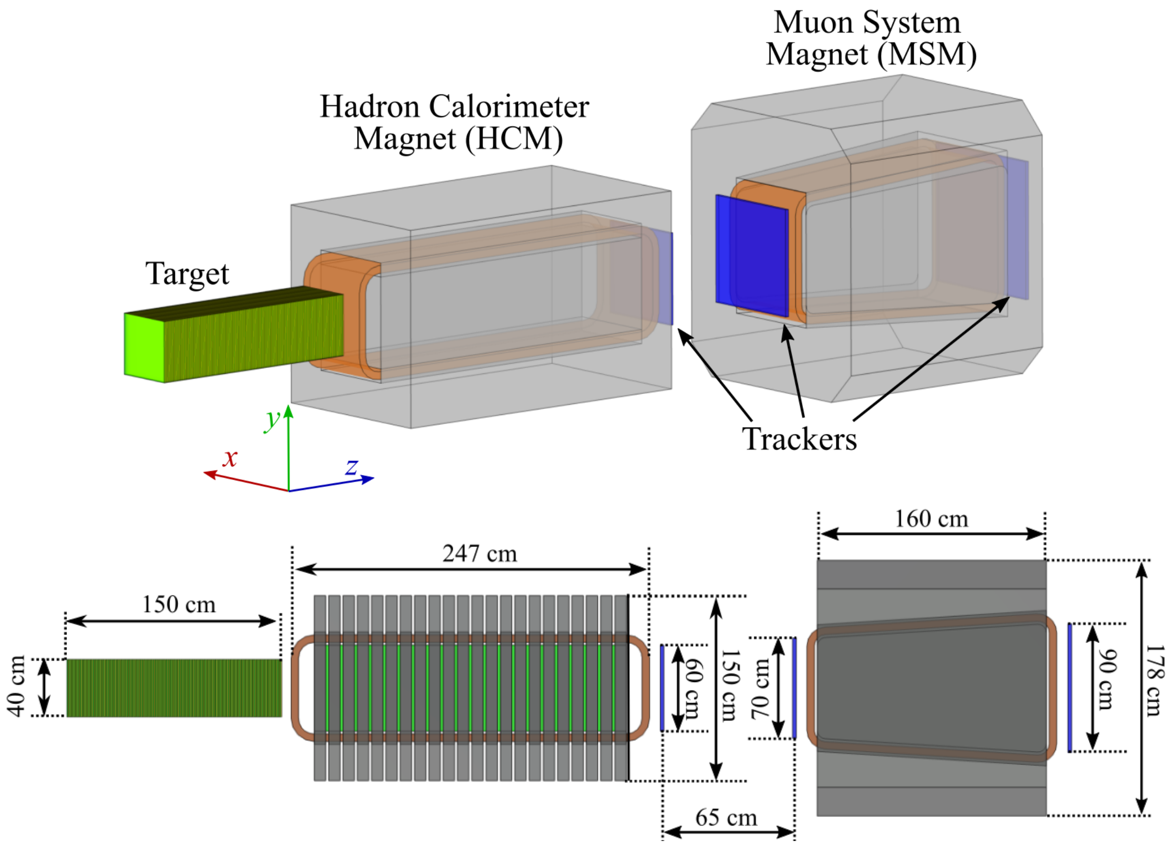

Figure 1. Schematic layout of the proposed integrated magnetic system for the upgraded SND@LHC detector for H-L LHC. Top: 3-D view; bottom: side view with dimensions.

Civil engineering is planned to accommodate the upgraded SND@LHC detector, including enlarging the tunnel and rerouting the existing ventilation ducts, cable trays, and drainage systems. Minimizing the overall dimensions of the spectrometer system is necessary to minimize the costs associated with civil engineering works: a sketch of the integration of the upgraded SND@LHC apparatus is presented in figure 2(a). The assembly of the magnet will have to be done on site, given the difficulty in the transportation. Indeed, the closest access to the LHC tunnel is through building 2155, as shown in the bottom drawing of figure 2. Moreover, the transportation path foresees walking along the tunnel for about 500 m and crossing the LHC machine in UJ18 to reach the TI18 tunnel. The crossing of the LHC machine requires either sliding the pieces underneath the machine or lifting them through the small hoist available. Hence the need to decompose the magnet into pieces and the limits on the size and weight of each piece. Nevertheless the location allows profiting from the LHC as a neutrino factory, in particular making measurements with neutrinos coming from decays of charmed hadrons [4]. The expected momentum distribution of muons from muon neutrino interactions in the upgrade of the SND@LHC detector is shown in figure 3, normalized to an integrated luminosity $L = 1\,\mathrm{fb}^{-1}$.

2.1 Physics goals and requirements

The main parameters used to define the spectrometer specifications are the muon momentum resolution and the geometrical acceptance, i.e. the fraction of muons which are fully reconstructed by the tracking

2024 JINST 19 P12002

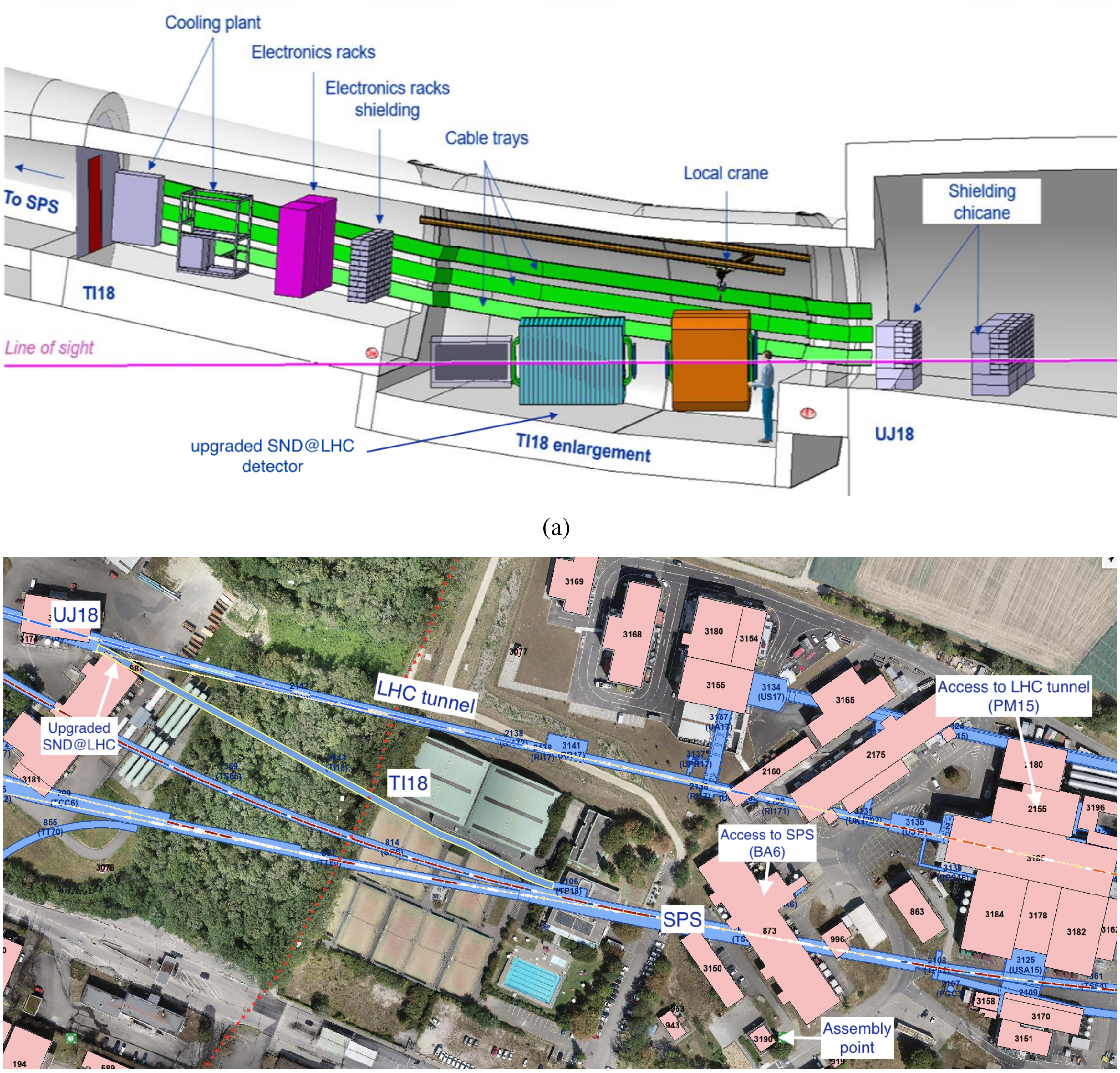

(a)

(b)

Figure 2. Sketch of the integration of the upgraded SND@LHC detector in the TI18 tunnel. Civil engineering works, required to accommodate the detector in the tunnel, are highlighted, such as the TI18 enlargement and rerouting of services (a). Map of the area around the LHC (b): the TI18 tunnel where the upgraded is foreseen to be placed as well as access points.

stations. These two parameters improve, respectively, increasing the length and the cross-section of the spectrometer, which is constrained by the available space in the TI18 tunnel. Moreover, safety rules and the vicinity to LHC impose limitations on the stray field.

The magnetic spectrometer system design can be regarded as a constrained optimization problem, with the muon momentum resolution maximization as the primary goal. Beside the momentum resolution, ancillary goals are to minimize the overall cost, the power consumption and usage of raw materials, aiming for the most sustainable option. The design variables are the geometrical parameters, such as the shape and size of the magnets, the coil configuration and yoke thickness, number of coil turns, as well as the H–B magnetic characteristic working point.

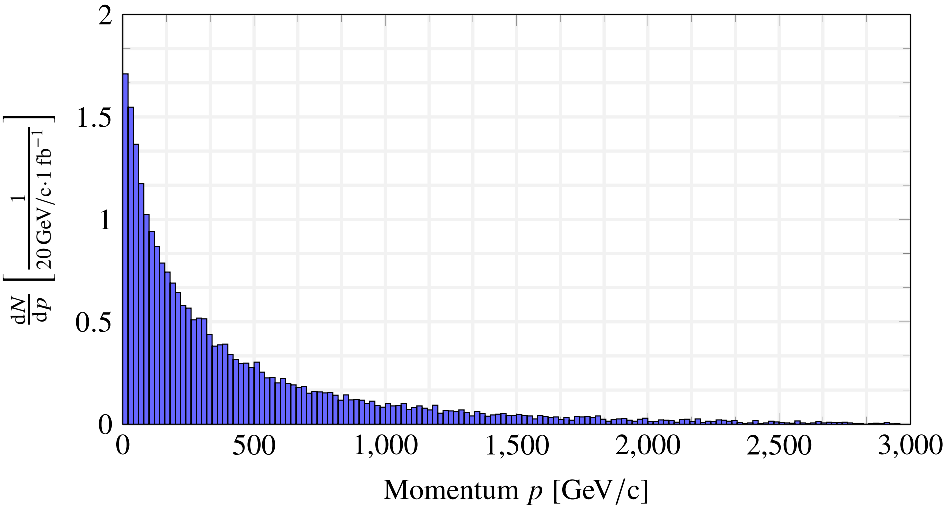

Figure 3. Expected muon momentum distribution from muon neutrino charged current (CC) interactions in the upgraded SND@LHC detector for an integrated luminosity of 1 fb^{-1}.

The constraints are:

1. geometrical physics acceptance above 90%;
2. major limitations to magnetic system size and shape, due to available space in the tunnel, minimizing civil engineering;
3. stray field compliant with safety regulations to allow human interventions in the proximity of the detector, and to avoid the interference with the LHC [5, 6].

The required magnet acceptance is accommodated by adapting the spectrometers' upstream and downstream apertures to the expected muon track origin and angles from the neutrino interactions in the target region. Given the required integrated bending field, the minimization of the detector length is primarily tackled by already magnetizing the hadronic calorimeter. Both magnet systems are proposed with iron cores in order to minimise the magneto-motive force and hence the power consumption for a given field. Hence the calorimeter is made of iron slabs interleaved with sensitive detector layers. The muon system magnet may also be filled with an iron core since the effect of multiple scattering on the momentum resolution is small at the LHC energies. As a result, the required electrical power is about three orders of magnitude less than the corresponding air-core solution. Moreover, the resulting low heat dissipation makes air cooling a viable solution, as it will be discussed in detail below. Figure 4 schematically shows the structure of the whole detector. In particular the proposed MSM configuration belongs to a new magnet class, referred to as *flux-symmetric conical magnets*, which considerably reduces the total volume of magnets with a sloping core, without relevant drawbacks [7]. In the specific MSM case, the magnet core is pyramidal-frustum shaped.

2.2 Operational and assembly constraints, and CERN standards

The upgraded SND@LHC experiment is expected to operate during the High Luminosity phase of the LHC, projected to start operation from 2029 [8]. The SND@LHC spectrometer system is

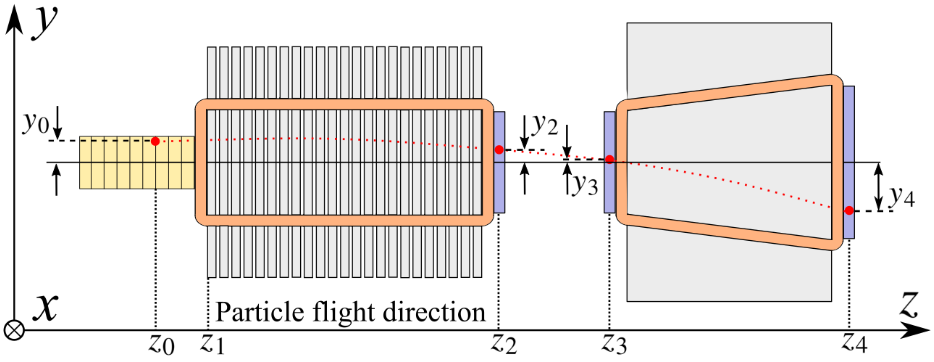

Figure 4. Schematic representation of the upgraded SND@LHC detector and dimension parameters. The detector is composed of the neutrino target, the Hadron Calorimeter Magnet (HCM), the Muon System Magnet (MSM) with three tracking stations. A possible trajectory of a muon crossing the detector is represented by the red dotted line.

expected to be permanently in operation throughout each year of data taking for up to ~9 months per year, including the commissioning phase.

Assuming that the upgraded SND@LHC experiment will profit from the entire duration of the HL-LHC, the spectrometer will need to guarantee ten years of operation, i.e. 90 months. Maintenance is possible during the planned year-end technical stops, lasting typically three months per year, and during the longer 1–2 year stops every 3–4 years. For other accesses to the detector during the operational year with the magnet powered, the magnet's design must comply with CERN safety regulations for human interventions in the proximity of magnetic fields [5, 6].

Given the complexity of access to the experimental area, as discussed above, the scenarios for the assembly of the upgraded SND@LHC spectrometer system will be detailed in further design phases.

3 Electromagnetic design and optimization

3.1 Detector performance and geometrical requirements

In this section we briefly describe how the momentum is estimated using the measurement of the particle position and how the momentum resolution is evaluated.

Consider again the layout of the spectrometer, as shown in figure 4. Muons produced in the neutrino target are primarily detected in the neutrino target itself and, successively, by the tracking stations located immediately after the calorimeter, and upstream and downstream of the muon system magnet.

The magnetic field deflects the muon, and its displacement, for a magnetic flux density B, is given at the first order by

$$\Delta y = \theta_y \, \Delta z + \frac{qB}{2p} \Delta z^2 + \Delta y_\sigma \tag{3.1}$$

where θ_y is the angle of the muon momentum with respect to the z-axis, p and q are, respectively, the muon momentum and charge, Δz is the length traveled in the magnetic field, and Δy_σ is the expected displacement due to the scattering in the material (tungsten, copper or iron).

The equation (3.1) is re-written for each part of the detector (with or without magnetic flux density). A linear combination of such equations gives, after some algebra, the momentum in the form

$$\frac{1}{p} = \frac{2}{q} \frac{z_{02}y_4 - z_{02}y_3 - z_{34}y_2 + z_{34}y_0 - \sigma}{z_{02}z_{34}[z_{34}B + (z_{12} + 2z_{01})B f_{\mathrm{HC}}]} \tag{3.2}$$

where $z_{ij} = z_j - z_i$ is the distance between the j-th and the i-th tracker, x_i is the position at the i-th tracking plane, f_{HC} is the filling factor of the calorimeter and σ is a linear combination of the displacements due to scattering. The quantity between square brackets in equation (3.2) is the total bending power of the spectrometer. By reciprocating equation (3.2), the momentum is estimated as

$$\hat{P} = \frac{q}{2} \frac{z_{02}z_{34}[z_{34}B + (z_{12} + 2z_{01})B f_{\mathrm{HC}}]}{z_{02}y_4 - z_{02}y_3 - z_{34}y_2 + z_{34}y_0} \tag{3.3}$$

where σ is removed since it has zero average. Note that the first position y_0 is measured in the neutrino target, where layers of passive material and high spatial resolution trackers are alternated.

There are three main sources of error in the measurement of the momentum: (*i*) the energy loss, (*ii*) the deflection due to the multiple scattering of the muon, (*iii*) the finite position resolution of the trackers.

Energy loss mostly affects the low energy muons and causes an underestimate in the momentum measured. The impact on the momentum resolution from multiple scattering is independent of the muon momentum to first order. Finally, the finite resolution of the trackers introduces an additive error on the measured displacements y_i. The intrinsic detector resolution mostly affects high momentum muons with momenta up to 1000 GeV/c, which is the relevant range for the experiment purpose.

The momentum resolution is straightforwardly defined as the ratio between the standard deviation of the momentum measurement and the momentum value, i.e. $\Delta p/p$. While its precise evaluation requires a numerical integration, a reasonably good approximation is obtained using a first order approximation of equation (3.2), which yields

$$\frac{\Delta p}{p} = \frac{2}{q} \frac{\sqrt{\varepsilon_s^2[2z_{02}^2 + z_{34}^2] + \varepsilon_t^2 z_{34}^2 + \sigma_\Sigma^2(p)}}{z_{02}z_{34}[z_{34}B + (z_{12} + 2z_{01})B f_{\mathrm{HC}}]} \tag{3.4}$$

where ε_t^2 and ε_s^2 are, respectively, the variance of the measurement error of the trackers in the target and around the magnets, and $\sigma_\Sigma^2(p)$ is the variance of the error caused by the scattering.

The first order approximation provides accurate values of the resolution up to $\Delta p/p \approx 0.2$, but it underestimates $\Delta p/p$ for higher values.

The derivation of σ_Σ^2 in equation (3.4) is out of the scope of this work, and is presented in reference [9]. We report here the formula

$$\sigma_\Sigma^2 = \frac{P_0^2}{p^2} \left[\frac{z_{34}^2}{3} \left(\frac{z_{01}^3}{X_{\mathrm{W}}} + \frac{z_{12}^3 + 3z_{01}z_{12}z_{02}}{X_{\mathrm{Fe}}} f_{\mathrm{HC}} \right) + \frac{z_{02}^2}{3} \frac{z_{34}^3}{X_{\mathrm{Fe}}} \right] \tag{3.5}$$

where $P_0 = 15$ MeV/c is an empirical constant, X_{W} and X_{Fe} are the radiation lengths of the tungsten and the iron, respectively.

Using equation (3.4), it is easy to show that the resolution improves with the magnetic field strength and the length of the magnetized regions. Since the calorimeter's length, the gap length and the total length are fixed, the muon system magnet can, at best, fill-up the remaining length.

2024 JINST 19 P12002

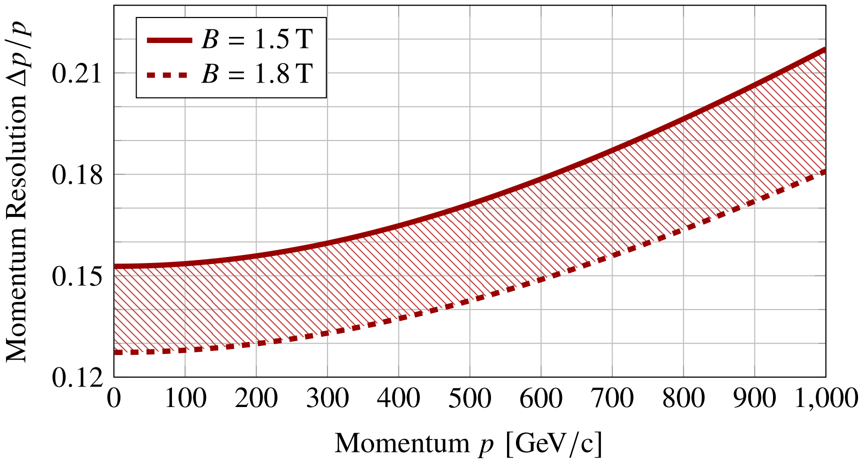

Figure 5. Momentum resolution as function of the muon momentum computed with the first-order approximation. The region between the solid lines and the dashed lines represent, respectively, the resolution between $B = 1.5\,\mathrm{T}$ and $B = 1.8\,\mathrm{T}$.

The plot of the expected resolution is shown in figure 5, for $z_{12} = 218\,\mathrm{cm}$, $z_{34} = 160\,\mathrm{cm}$, $\varepsilon_s = 140\,\mu\mathrm{m}$, and $\varepsilon_t = 100\,\mu\mathrm{m}$. The actual resolution is expected to be slightly worse than the prediction of the first order approximation [9], nonetheless the plot shows that fields in the range 1.5 T–1.8 T can achieve a resolution better than 25% for muon momenta up to 1000 GeV/c. Further considerations on the chosen magnetic flux density are presented in the next sections.

3.2 Design optimisation

In the following we assume that the two iron core magnets are sufficiently separated to neglect the reciprocal magnetic interaction, allowing us to carry out separate electromagnetic analysis. This assumption is easily verified a-posteriori after the full electromagnetic analysis is carried out due to the extremely low stray fields. Following the approach given in reference [10], we introduce here the problem formulation, the scalings and the analytical formulas useful for optimizing the muon system magnet.

3.2.1 Iron core magnetic properties and models

The iron core magnet, as proposed, requires carefully choosing the iron quality with cost versus performance in mind, as well as proper modeling in the field simulation in order to correctly predict the relevant region of the field map. Concerning the real magnetic characteristics of the candidate iron types, we adopt the same conservative assumptions as done in [10]. We recall that, among the yoke materials used at CERN there are, in order of performance (and cost), low carbon steels, such as AISI 1010 [11], special grade low carbon steels of relatively high purity, such as ARMCO® Pure Iron grade 4 [12], and cobalt iron. Reference [13] reports H–B curves of materials used as magnetic steel as obtained from measured samples, in particular for different heats of the AISI 1010 steel and a special grade. We consider their upper and lower bounds on the field strength B, which are labelled ARMCO ATLAS and ST 1010 ATLAS [14] in reference [13]. Figure 6 shows the H–B characteristic for those two bounding materials. Clearly, for a given desired B in the magnet core, the corresponding H, and hence the required electric current and power consumption, are rather different in the two cases.

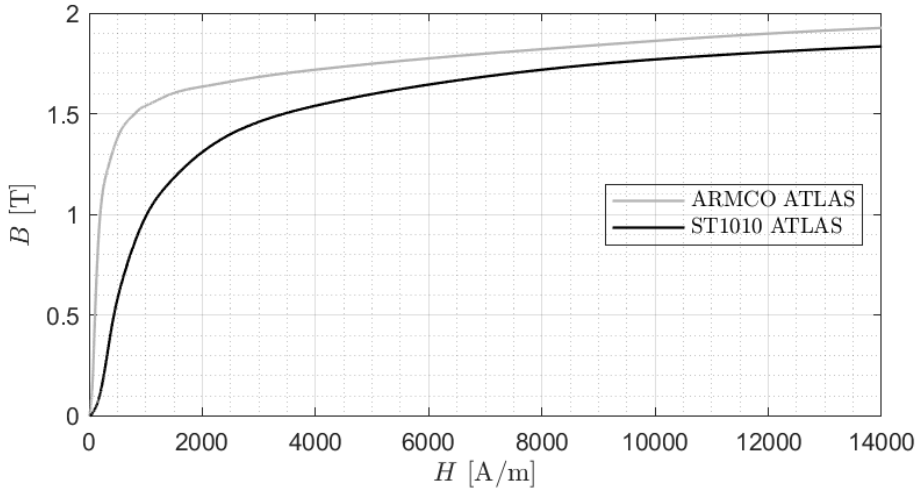

Figure 6. Best case (ARMCO ATLAS) and worst case (ST1010 ATLAS) H–B characteristic of iron materials commonly used to build experimental magnets, obtained from measured samples [13]. The latter is used for all our analyses, as it implies a robust and less expensive design. Reproduced from [13]. CC BY 3.0.

While ARMCO is clearly a superior material, it is significantly more expensive. Given the limited power consumption of both the HCM and MSM magnets (of the order of 1–2 kW each, see tables 1–2), a low cost iron choice is viable. Therefore we will consider AISI 1010 or an European equivalent grade. Moreover, we orient our design toward weakly saturated iron mode, still in non-linear region, in order, from one side, to relax the magnetic induction density uncertainties in the realization and, on the opposite side, limit too high stray fields outside the magnet. This corresponds to $H \approx 9$ kA/m, where most of the H–B curves of the mentioned AISI 1010 heats, including ST1010 ATLAS (figure 6), converge to the same range of values of the flux density, that is $B \approx 1.7$ T [13].

Note that the character just described of H–B curves, in particular the reduced variability for $B \gtrsim 1.7$ T within a family of various heats of a certain kind of iron, is not specific of just AISI 1010, but is valid more in general, as reported for instance for the iron type used for the OPERA Magnetic Spectrometer, which is a S235 JR steel, UNI EN 10025 compliant, with prescribed impurity content [15, 16]. The above considerations lead us to choose AISI 1010 or an European equivalent grade as material and to use, for all our subsequent analyses, the H–B curve for ST1010 ATLAS shown in figure 6, which correspond to the worst case scenario.

3.2.2 Muon System Magnet design

We analyze the Muon System Magnet first, as the corresponding results are also applicable to the Hadron Calorimeter Magnet. For the MSM we propose a particular configuration that makes it belong to a new magnet class that we call *flux-symmetric conical magnets*. Such a configuration, which for the specific MSM case is pyramidal-frustum shaped, is specifically conceived for magnets with sloping cores to minimize their total volume, as briefly reported further below and more in general in reference [7].

To determine the flux balance we neglect the stray flux which, for reasonable values of the maximum stray flux density B^*_{stray} on the surface of the yoke (of $O(10)$ mT), typically results in a few percent error. In this respect, we note that the internal sloping traits of the coil do not contribute to the flux balance, since B_x symmetrically changes sign when moving vertically across the coil

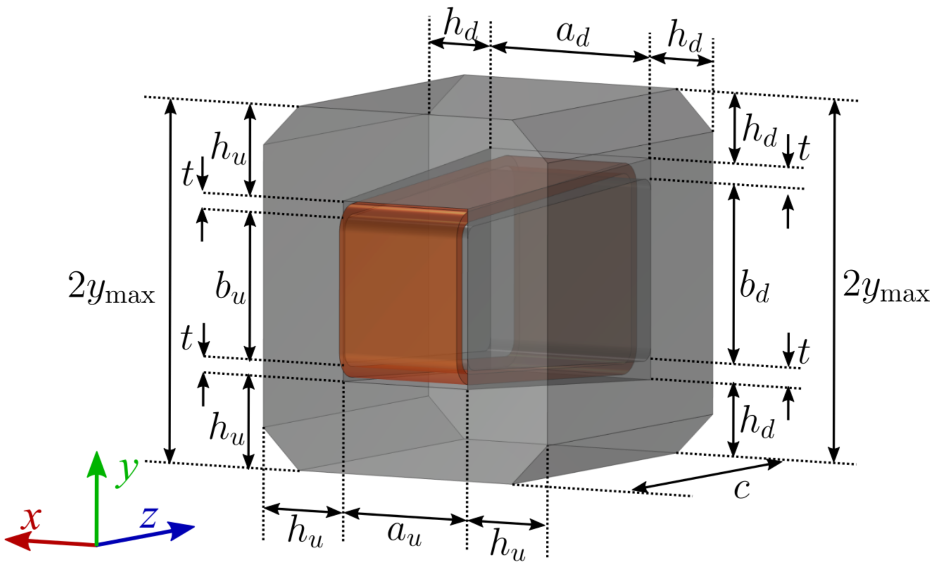

Figure 7. Three dimensional representation of the *pyramidal-frustum-shaped flux-symmetric* [7] Muon System Magnet and definition of the geometrical parameters relevant for the analytical and numerical analyses.

traits. The flux balance is then obtained by considering the flux across the two net iron surfaces (core and return yoke) defined by virtually cutting the magnet along the plane $x = 0$. The net iron surfaces have trapezoidal shapes (see figure 4 and figure 7). The approximate balance equation reads as $\frac{(b_{\mathrm{u}}/2+b_{\mathrm{d}}/2)c}{2}B = \frac{(h_{\mathrm{u}}+h_{\mathrm{d}})c}{2}B_{\mathrm{ret}}$, where the subscripts u and d stand for upstream and downstream, and B and B_{ret} are the reference flux density in the core and the flux density in the return yoke, respectively. We then consider the average quantities

$$\bar{a} = \frac{a_{\mathrm{u}} + a_{\mathrm{d}}}{2}, \quad \bar{b} = \frac{b_{\mathrm{u}} + b_{\mathrm{d}}}{2}, \quad \bar{h} = \frac{h_{\mathrm{u}} + h_{\mathrm{d}}}{2},$$

that correspond geometrically to the centre of the magnet ($z = 0$). The resulting flux balance is then

$$\bar{b}B = 2\bar{h}B_{\mathrm{ret}} \,. \tag{3.6}$$

The name *flux-symmetric* refers to achieving the flux balance by considering a design where the top surface of the two mentioned surfaces is a doubly-mirrored version of half of the one corresponding to the core, and both those surfaces have quite similar areas. The main advantage of the flux-symmetric configuration is in the volume minimization. This becomes clear when comparing it with the ‘canonical’ or ‘natural’ *fully conical* design, as discussed in reference [7].

The motivation to consider the latter lies in the fact that it should ‘naturally’ provide a less distorted field configuration. However, in practice the flux-symmetric design does not convey sensible performance degradation and hence it is preferred here since it is more compact. See section 3.3 for the quantitative details concerning the field quality of the flux-symmetric configuration and reference [7] for a comparison with the canonical design. Also notice that *the flux-symmetric conical* configuration has a general character. In particular, the word ‘conical’ is meant to state that the cross-section can be of any shape, e.g. a circle, an oval or a polygon and, moreover, the concept is applicable to magnets with air core too.

The magneto-motive force $\mathcal{F} = NI$ required to obtain a flux density B in the core is approximately

$$\mathcal{F}(B) = NI(B) \cong \bar{a}\mathcal{H}(B) + \ell_{\mathrm{MSM}}\mathcal{H}(B_{\mathrm{ret}}) = \bar{a}\mathcal{H}(B) + \ell_{\mathrm{MSM}}\mathcal{H}\left(\frac{bB}{2h}\right) \tag{3.7}$$

where

$$\ell_{\mathrm{MSM}} = \bar{a} + 2\left(\frac{\bar{b}}{4} + t\right) \tag{3.8}$$

and $H = \mathcal{H}(B)$ defines the nonhysteretic nonlinear characteristic of the type of soft iron chosen for the yoke, labeled as ST1010 ATLAS in figure 6. Equation (3.8) is adapted from reference [10] by considering that in the present case the magnet has an iron core instead of an air core and B is intended as the mean of the flux density in the core.

The exact and approximate mean length per turn of the coil winding are

$$\begin{aligned} l_{\mathrm{t}} &= b_{\mathrm{u}} + b_{\mathrm{d}} + 2d - 2r_{\mathrm{in}}\left(4\frac{d}{c} - \pi\right) + \pi t \\ &\cong b_{\mathrm{u}} + b_{\mathrm{d}} + 2c \end{aligned} \tag{3.9}$$

where r_{in} is the inner radius of the arc parts of the coil, taking also into account the thickness of the resin and of the additional insulator and ancillary parts, and $d = \sqrt{c^2 + \left(\frac{b_{\mathrm{d}} - b_{\mathrm{u}}}{2}\right)^2}$ is the hypotenuse of the trapezoid representing the inner iron core (figure 4). This corresponds to the virtual case in which the corners are not rounded, $r_{\mathrm{in}} = 0$. In our specific case it is $\frac{d}{c} \cong 1.002$ and the approximate expression of l_{t} in equation (3.9) underestimates its exact value by about 3%.

The minimum value of r_{in}, required to avoid the keystone effect on the conductors, is specified in terms of the geometry of the conductor itself. Specifically, if a_{cond} is the edge length of the conductor cross-section in the horizontal direction and $r_{\mathrm{Cu\,min}}$ is the minimal bending radius of the conductor (note that $r_{\mathrm{Cu\,min}} = r_{\mathrm{in}}$ + additional thicknesses, as stated), for copper conductors the keystone effect is considered small (less than 3.6% in relative terms) when $r_{\mathrm{Cu\,min}} > 3a_{\mathrm{cond}}$ [17]. We also recall that for conductors made of aluminum, the latter condition may be less strict [18, 19].

The current density, the volumetric power density and the net volume occupied by the electrical conductor are $J = \frac{\mathcal{F}}{f a_{\mathrm{u}} t}$, ρJ^2 and $\Omega = f a_{\mathrm{u}} t l_{\mathrm{t}}$, respectively, where f is the global coil filling factor (which takes into account insulators and ancillaries) and ρ is the electrical resistivity of the conductor. The electrical power consumption is then

$$P = \frac{\rho(T) l_{\mathrm{t}} \mathcal{F}^2}{f a_{\mathrm{u}} t} \tag{3.10}$$

where the dependence of the resistivity on the temperature is marked. In the hypothesis of the other parameters being constant, equation (3.7) allows expressing P approximately as a function of the core reference flux density B (figure 8). The maximum stray flux density B^*_{stray} on the top and lateral surface of the iron (evaluated at symmetry points [10]) is given by

$$B^*_{\mathrm{stray}} = \mu_0 H^*_{\mathrm{stray}} = \frac{B_{\mathrm{ret}}}{\mu_{\mathrm{r}}(B_{\mathrm{ret}})}\,. \tag{3.11}$$

The coil is made with 42 turns of copper conductor having cross-sectional area of 26 × 26 mm^2. This choice implies two facts: (i) the current density J is sufficiently low so that air-cooling is possible and (ii) power converters of a certain CERN standard class can be used, see section 4.1.

2024 JINST 19 P12002

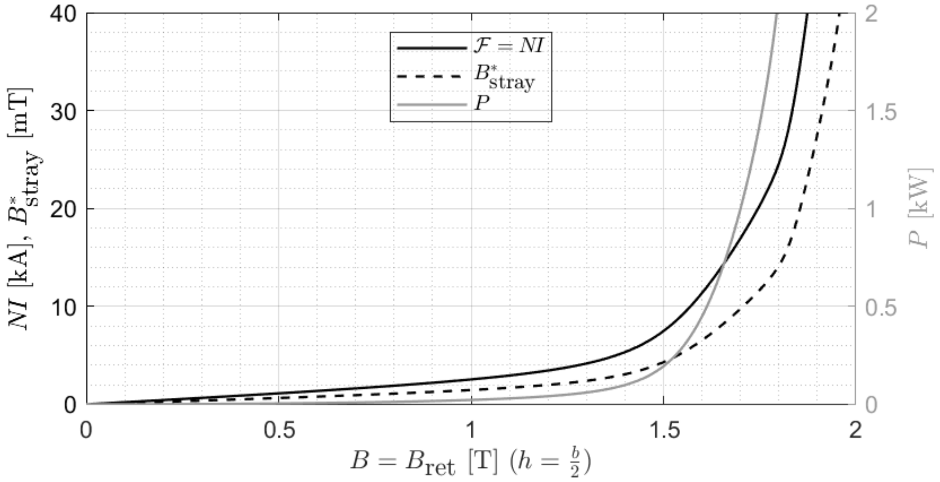

Figure 8. Magnetomotive force $\mathcal{F}$, maximum stray flux density (on the top and lateral surface of the iron) $B^*_{\rm stray}$ and power consumption P, for the Muon System Magnet as a function of the reference flux density B in the core, in the case $\bar{h} = \frac{\bar{b}}{2}$ and assuming the other parameters are constant (e.g. the coil thickness t). The corresponding curves for the Hadron Calorimeter Magnet are qualitatively the same as the ones shown here, with quantitative differences mainly due to the different core cross-section and different N and $l_{\rm t}$ values.

Table 1 reports the main parameters of the Muon System Magnet. Figure 8 shows $\mathcal{F}$, $B^*_{\rm stray}$ and P for the Muon System Magnet as a function of B, in the case $h = \frac{b}{2}$ (to which corresponds $B_{\rm ret} = B$) and assuming the other parameters as in table 1.

3.2.3 The Hadron Calorimeter Magnet design

The Hadron Calorimeter Magnet is much simpler to analyze as it has parallelepipedal geometry. The formulae reported above for the MSM remain valid, provided that a, b and h are used in place of $\bar{a}$, $\bar{b}$, $\bar{h}$, etc. The mean length per turn in particular becomes

$$\begin{aligned} l_{\rm t} &= 2b + 2c - 2r_{\rm in}(4-\pi) + \pi t \\ &\cong 2b + 2c \end{aligned} \tag{3.12}$$

where

$$c = 22\Delta c_{\rm Fe} + 21\Delta c_{\rm D}\,,$$

and $\Delta c_{\rm Fe}$, $\Delta c_{\rm D}$ are the thicknesses of the iron slabs and of the air gaps aimed at housing the scintillating bar planes. In the expression for $\mathcal{F}$, equation (3.7), the quantity $\ell_{\rm HCM} = a + 2\left(\frac{b}{4} + t\right)$ has to be used in place of $\ell_{\rm MSM} = \bar{a} + 2\left(\frac{\bar{b}}{4} + t\right)$. Table 2 reports the main parameters of the Hadron Calorimeter Magnet.

3.3 3-D electromagnetic analysis

In this section a full 3-D numerical analysis of the two components of the magnetic detector system is given. A Finite-Element Method (FEM) formulation based on edge elements and a non-gauged magnetic potential vector formulation [20, 21] have been employed to find the DC steady-state magnetic nonlinear solution for the total field through the Magnetic Fields interface of the AC/DC module of the COMSOL Multiphysics® [22] software package. Boundary conditions have been imposed by infinite elements. The numerical solution of the non-linear equation system has been obtained using a flexible

Table 1. Main parameters of the Muon System Magnet. The subscripts u and d stand for upstream and downstream, respectively (see figure 7).

Description		Symbol(s)	Value
Total magnetized longitudinal iron length	[m]	c	1.60
Total cross-section (both upstream and downstream)	[m^2]	$2x_{\max} \times 2y_{\max}$	1.60×1.78
Core upstream cross-section	[m^2]	$a_\mathrm{u} \times b_\mathrm{u}$	0.70×0.70
Core downstream cross-section	[m^2]	$a_\mathrm{d} \times b_\mathrm{d}$	0.90×0.90
Core mid cross-section ($z = 0$)	[m^2]	$\bar{a} \times \bar{b}$	0.80×0.80
Return yoke thickness [upstream mid downstream]	[m]	$[h_\mathrm{u}, h, h_\mathrm{d}]$	$[0.45, 0.40, 0.35]$
Total coil thickness (including dampers/insulators)	[mm]	t	92
Conductor cross-section	[mm^2]	$a_\mathrm{cond} \times b_\mathrm{cond}$	26×26
Total number of turns	[—]	N	$2 \times 21 = 42$
Inner coil curvature radius (see text after eq. (3.9))	[mm]	r_in	90
Mean turns length	[m]	l_t	5.0
Total conductor length	[m]	Nl_t	208
Reference flux density (magnetized sloping core)	[T]	B	1.75
Field in-homogeneity @ 94% volume	[%]	$\Delta B/B$	≤ 3
Stray field [@ iron surface, @ $d > 2$ m]	[mT]		$[\lesssim 10, \lesssim 1]$
Voltage at the coil terminals	[V]	V	3.0
Electrical current	[A]	I	500
Current density	[A/mm^2]	J	0.74
Magnetomotive force	[kA]	$\mathcal{F} = NI$	21.0
Electrical power	[kW]	P	1.5
Total conductor mass	[t]	m_Cu	1.25
Total iron mass	[t]	m_Fe	33

generalized minimum residual method (FGMRES iterative solver). For the solution of each linear step, an iterative method based on the geometric multi-grid coupled with a successive over-relaxation (SOR) pre-smoother and post-smoother has been used. Before performing the steady-state study, a coil geometry analysis through a COMSOL built-in tool has been preliminarily performed in order to compute the current flowing within the coil elements.

As discussed in section 3.2.1, the H–B curve we use for all simulation is the ST 1010 ATLAS shown in figure 6.

3.3.1 The Muon System Magnet

In order to reduce the computational burden, the symmetry of the geometrical and physical problem has been exploited and only one quarter of the whole structure has been modeled (figure 9(a)).

Figure 10 reports the mesh used for the Finite-Element (FE) analysis. For the discretization of the coil, iron yoke and surrounding air domains, tetrahedral elements are employed. In particular, in figure 10(a) it can be seen that the surrounding air domain has been limited to a sphere with a radius of 6 m whereas externally an infinite boundary layer has been considered [22]. This is the reason why the outermost region has not been meshed. Figure 10(b) provides, instead, a detail of the inner region of

Table 2. Main parameters of the Hadron Calorimeter Magnet (HCM).

Description		Symbol(s)	Value
Total longitudinal length (iron + gaps + coil)	[m]	l_{igc}	2.54
Total magnetized longitudinal iron core length	[m]	$22\Delta c_{\mathrm{Fe}}$	1.76
Total cross-section	[m^2]	$2x_{\max} \times 2y_{\max}$	1.20×1.50
Core cross-section	[m^2]	$a \times b$	0.60×0.60
Return yoke thickness	[m]	h	0.30
Total coil thickness (including dampers/insulators)	[mm]	t	92
Conductor cross-section	[mm^2]	$a_{\mathrm{cond}} \times b_{\mathrm{cond}}$	26×26
Total number of turns	[—]	N	$2 \times 18 = 36$
Reference flux density (magnetized core)	[T]	B	1.76
Field in-homogeneity @ 98% volume	[%]	$\Delta B/B$	≤ 3
Stray field [@ iron surface, @ $d > 2$ m]	[mT]		[$\lesssim 10, \lesssim 1$]
Voltage at the coil terminals	[V]	V	3.1
Electrical current	[A]	I	500
Current density	[A/mm^2]	J	0.75
Magnetomotive force	[kA]	$\mathcal{F} = NI$	18
Electrical power	[kW]	P	1.5
Total conductor mass	[t]	m_{Cu}	1.3
Mass of a single iron slab	[t]	$\frac{m_{\mathrm{Fe}}}{22}$	1.02
Total iron mass	[t]	m_{Fe}	22.5

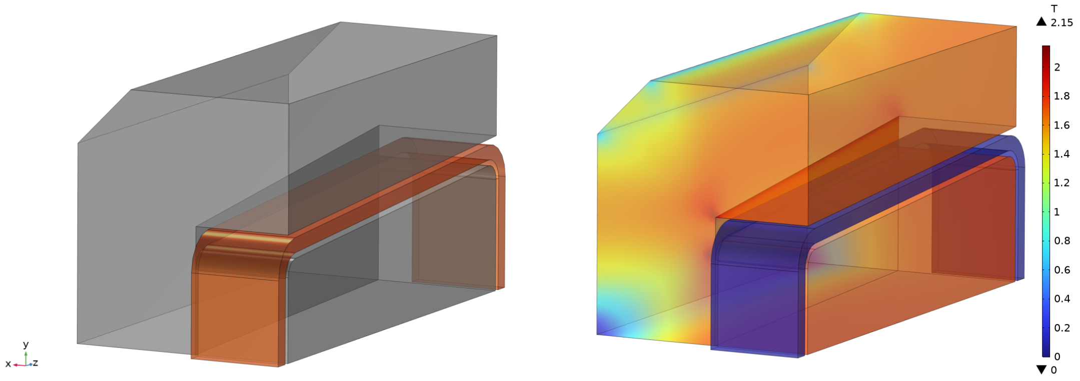

(a) (b)

Figure 9. (a) 3-D view of one quarter of the whole magnet: in grey, the iron yoke; in orange, the coil. The surrounding air domain is not sketched here. (b) Modulus of magnetic flux density (expressed in Tesla [T]) for the muon system magnet.

the mesh. The mesh approximately consists of 1.34 million elements of which 18 000 elements in the coil and 500 000 in the iron yoke, respectively. Figure 9(b) shows the 3-D distribution of the magnetic flux density norm $|B|$ within the active region (iron core), the iron yoke and the coil. Figure 11 shows the 2-D distribution of the magnetic flux density norm $|B|$ within the magnet and the surrounding air domain on the $x - y$ plane upstream (a) and downstream (b) of the magnet.

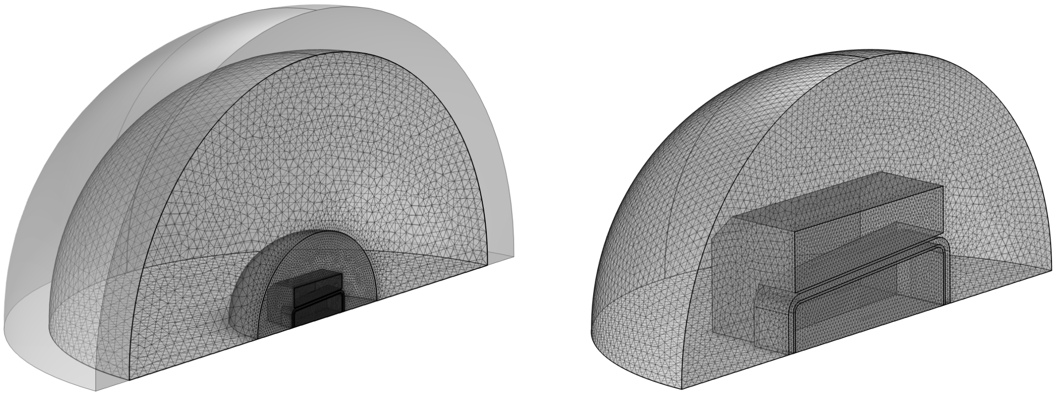

(a) (b)

Figure 10. Mesh used for FE analysis. On the left (a), the whole mesh. The outermost domain, which is made of air, is non-meshed since an infinite boundary layer has been employed. On the right (b), a detail of the mesh with the magnet and the innermost fine-meshed air domain.

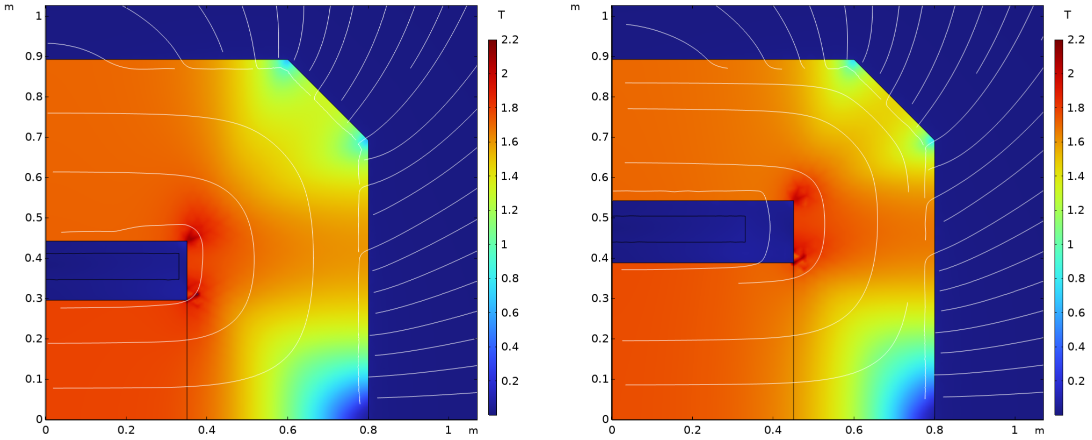

(a) (b)

Figure 11. The $|B|$ 2-D mapping in the $x - y$ plane upstream (left) and downstream (right) of the magnet. The point $(0, 0, 0)$ corresponds to the centre of the magnet.

In the active region (iron core), the average value of the desired magnetic flux density component along the x-axis is 1.75 T.

A synthetic but comprehensive figure of merit for the field uniformity can be defined as the variation $\Delta B/B$ in the whole active volume. The results provided by numerical analysis demonstrate that the field is within 3% of the desired level over more than 94% of the active volume, and that large distortions are only found at the very periphery of the active region. Figure 12 reports the distribution of the B_x component in the core, whereas figure 13(b) shows its line integral $\int_{z=-c/2}^{z=c/2} B_x\, ds$ distribution, where s is the arclength evaluated along a set of lines represented in figure 13(a). Such lines are defined by their initial (upstream) and final (downstream) points, respectively given by $(x_{\mathrm{u}i}, y_{\mathrm{u}j}, z_{\mathrm{u}}) = \left(\alpha_i \frac{a_{\mathrm{u}}}{2}, \beta_j \frac{b_{\mathrm{u}}}{2}, -\frac{c}{2}\right)$ and $(x_{\mathrm{d}i}, y_{\mathrm{d}j}, z_{\mathrm{d}}) = \left(\alpha_i \frac{a_{\mathrm{d}}}{2}, \beta_j \frac{b_{\mathrm{d}}}{2}, \frac{c}{2}\right)$, where $\alpha_i \in \{0, 0.2, 0.4, 0.6, 0.8, 1\}$ and $\beta_j \in \{0, 0.2, 0.4, 0.6, 0.8, 0.9, 1\}$. It is worth to underline that the integrals calculated values have been graphically reported to the upstream x–y cross-section.

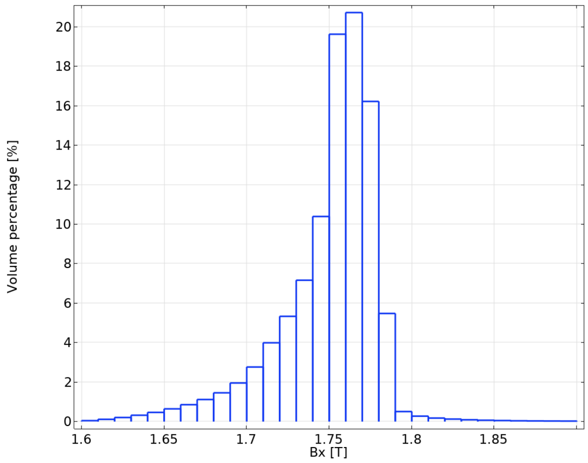

Figure 12. Volume distribution of magnetic flux density, x-component B_x within the active iron region.

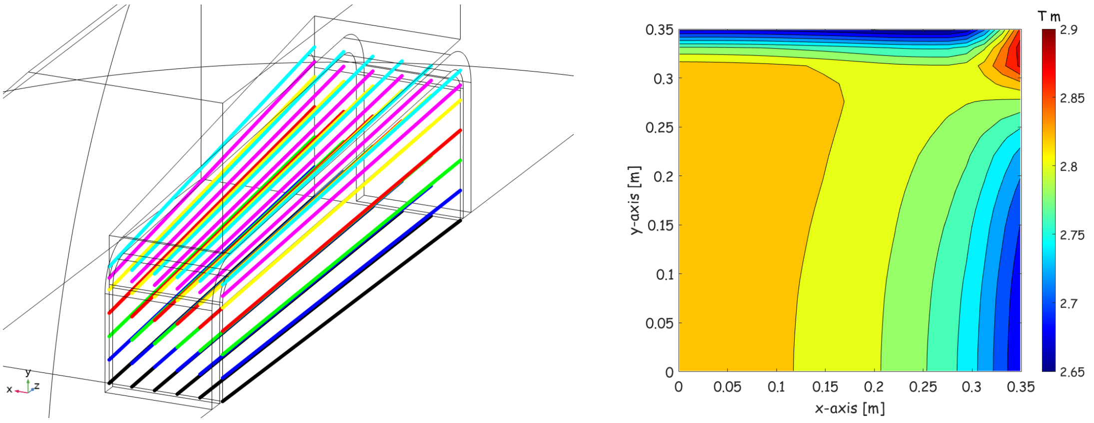

(a)

(b)

Figure 13. (a) Lines along which B_x has been integrated (muon system magnet). (b) Cross-section distribution of $\int_{z=-c/2}^{z=c/2} B_x \, ds$, s being the arclength along the lines (the values calculated along lines have been reported into the upstream x–y cross-section).

The 3-D FEM analysis allows evaluating the stray field outside of the magnet volume. Figure 14(a)–14(b) shows the distribution of the flux density in the planes $z = 0$ (a) and $x = 0$ (b), respectively. In particular, it can be seen that the norm of the stray flux density is anywhere lower than 25 mT, and its maximum value is attained right outside the coil, close to its vertical strokes. The fast decay of the stray flux density outside the magnet could also be appreciated in figure 14, the scale being logarithmic. As a general rule, a stray field smaller than 2 mT is expected at distance larger than 2 m from the magnet system.

3.3.2 The Hadron Calorimeter Magnet

The high degree of symmetry of the HCM magnet allows the computational burden to be reduced and the quality of the results to be improved by modelling only one eighth of the whole structure. The mesh used in the calculation consisted of 275 911 tetrahedral, 8 554 pyramidal and 155 568

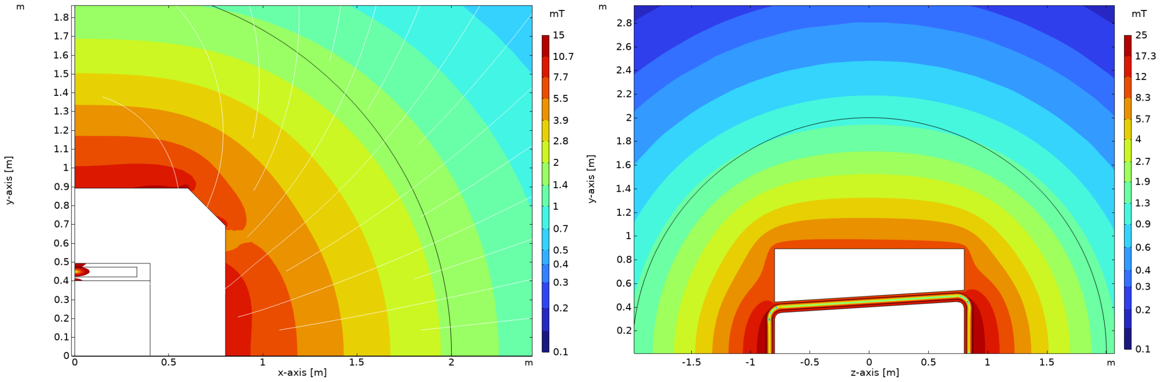

(a) (b)

Figure 14. Stray magnetic flux density, in modulus ($|\boldsymbol{B}|$), for the muon system magnet (expressed in [mT], logarithmic scale) within the external air domain in (a) $x - y$ plane at $z = 0$ and (b) $z - y$ plane at $x = 0$.

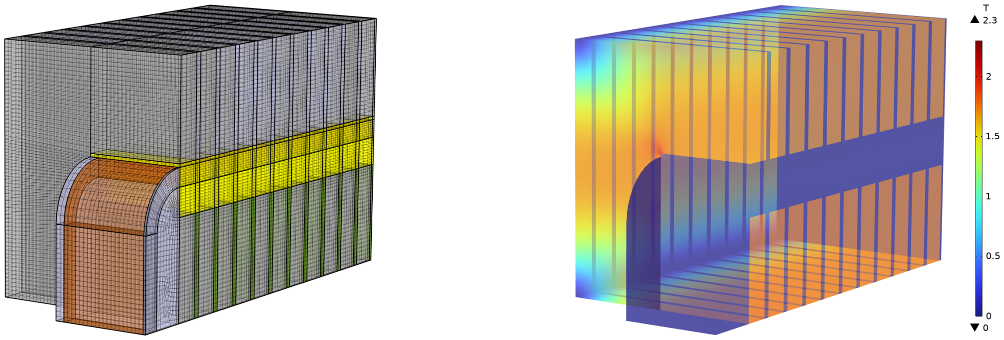

(a) (b)

Figure 15. Mesh of the HCM components: brown = coil, yellow = coil insulation and additional space for electronics; green: particle detectors; gray = iron core. Magnetic flux density for the calorimeter magnet (expressed in [T]).

hexahedral elements for a total of 5 645 868 unknowns. Figure 15(a) shows the FE model used for the HCM components.

In the assumed coordinate system, the active core region is limited in the area $0.3\,\mathrm{m} < x$, $y < 0.3\,\mathrm{m}$. The average value of the magnetic flux density x-component in this region is 1.76 T.

Figure 15(b) shows the 3-D distribution of the magnetic flux density norm $|B|$ within the active region (iron core), the iron yoke and the coil. Figure 16 shows the 2-D distribution of the magnetic flux density norm $|B|$ in the $x - y$ plane at $z = 0.055\,\mathrm{m}$.

Also for the HCM the field homogeneity has been analyzed in detail. The analysis here is more straightforward, since no frustum shape is involved. In figure 17(a) we show the distribution of $\Delta B/B$ in % in the active area plane, just to give a clear picture of it, evidencing the regions where it exceeds 3%. A further detail is evidenced in figure 17(b), where the region exceeding 3% is zoomed out: it shows how at the extreme corner such value increases to 14%. The same synthetic figure of merit previously defined for the field uniformity, i.e. the variation $\Delta B/B$ in the whole active volume, shows that the field is within 3% of the desired level over more than 98% of the active volume, and that large distortions are only found at the very periphery of the active region.

2024 JINST 19 P12002

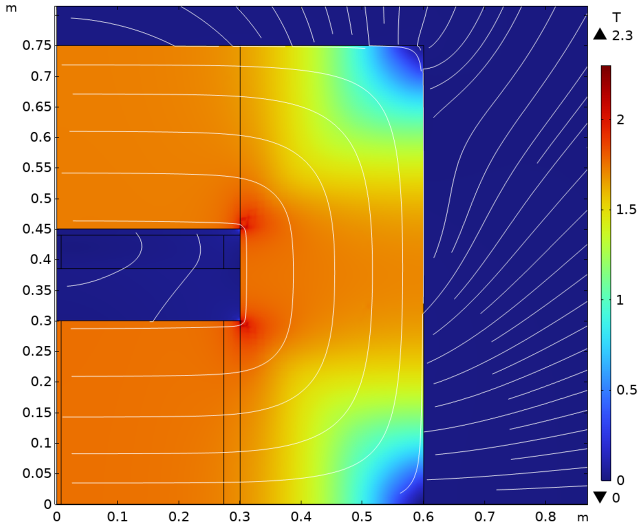

Figure 16. The $|B|$ 2-D mapping in the $x-y$ plane at $z = 0.055$ m. The point $(0, 0, 0)$ is the centre of the magnet.

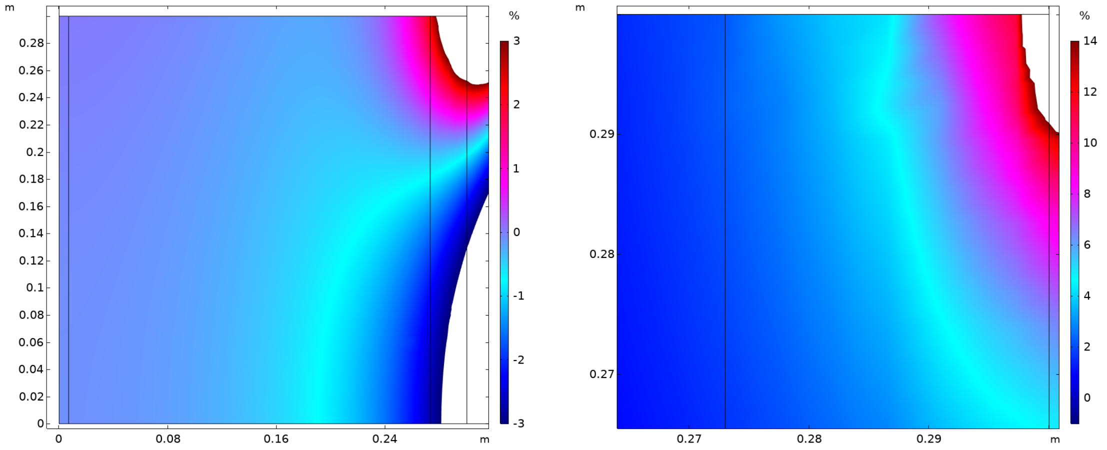

(a)

(b)

Figure 17. 2-D mapping of the $\Delta B/B$ ratio in the cross-section $z = 0.055$ m of the active region: (a) $\Delta B/B < 3\%$ high uniformity region (98% of the cross-section) and (b) detail of the remaining region $\Delta B/B > 3\%$ (2% of the cross-section).

Figure 18(b) shows the distribution of $\int_{-c/2}^{c/2} B_x\, dz$. In particular, the B_x component of the magnetic flux density has been integrated along the set of lines represented in figure 18(a). Such lines, that are parallel to the z axis and for which $z \in [-c/2, c/2]$, have coordinates in x–y the cross-section equal to $(x_i, y_j) = \left(\alpha_i \frac{a}{2}, \beta_j \frac{b}{2}\right)$, with $\alpha_i \in \{0, 0.2, 0.4, 0.6, 0.8, 1\}$ and $\beta_j \in \{0, 0.2, 0.4, 0.6, 0.8, 0.9, 1\}$.

As shown in figure 19(a), the maximum value of 15 mT for the stray magnetic field is attained at a distance of 2 cm from the vertical legs of the coil. At a distance of 1 m from the yoke, in the $x-y$ plane, the stray field is limited to 4–5 mT (see figure 19(b)). From the latter analysis, it can be concluded that no special effort is needed to reduce the stray field. Figure 19(a) shows also that in the air region between the two magnets, the maximum stray magnetic field is limited to about 5 mT at a distance of 1 m from the vertical leg of the coil.

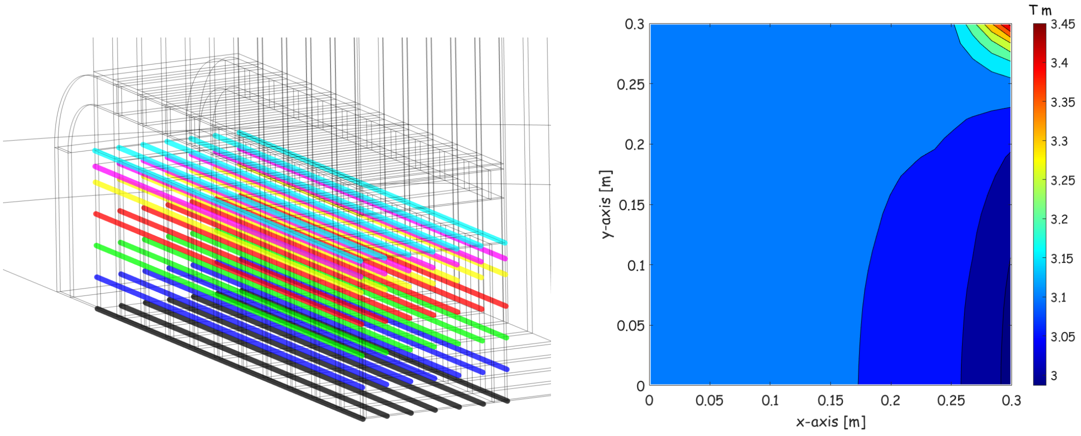

(a) (b)

Figure 18. (a) Lines along which B_x has been integrated (hadron calorimeter magnet). (b) Spatial distribution of $\int_{-c/2}^{c/2} B_x \, dz$.

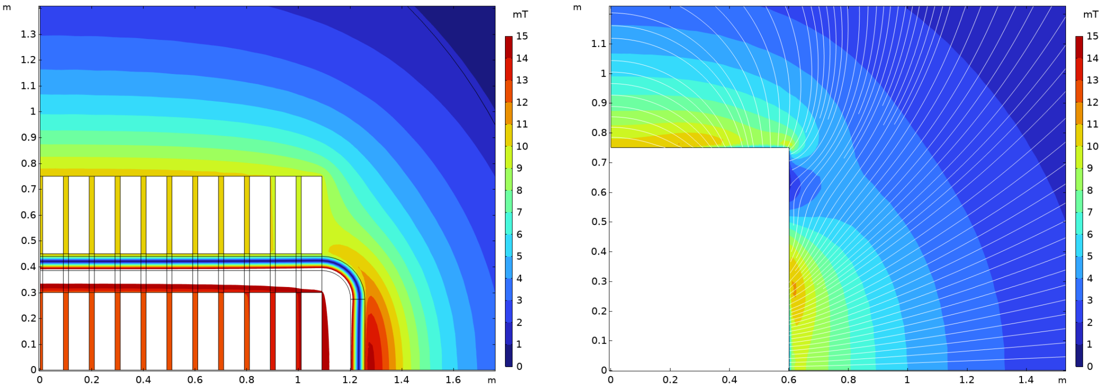

(a) (b)

Figure 19. 2-D mapping of the stray magnetic field in the cross-sections. (a) Longitudinal section at $x = 0$ and (b) transverse section at $z = 0$.

4 Complementary design aspects and cost estimate

4.1 Power converters

As stated in section 3.2.2, the coil has been designed so that air-cooling is possible (see below) and such that power converters of a certain CERN standard class can be used. The whole power converter system would then be composed of: (i) a single LHC600A-10V rack including two power converter slots running on FGC2 (Function Generator/Controller embedded controller) with four installed DC current transformer units (DCCT) [18, 23] for high accuracy current measurement, (ii) four LHC600A-10V power module units, two of which are needed in the rack plus two units as spares. Two DCCTs per converter module are used to improve reliability and minimize potentially destructive failures in case of an issue with the measurement accuracy of the DCCTs.

The LHC600A-10V converter type allows four-quadrant operation and its main nominal ratings are ±10 V, 600 A. Effective ratings to be considered to ensure controllability are then limited to ±9 V, 550 A.

The conductor chosen operates in DC at a fraction of the voltage, that is about 3 V (see tables 1–2). The voltage difference with respect to the rating is left for the ramp-up phase (turn-on transient).

The LHC600A-10V converter is water-cooled and is typically able to withstand a radiation absorbed dose up to 50 Gy, which is expected to be enough for the magnets lifetime, according to radiation measurements performed in the TI18 tunnel [24–26] and extrapolated to High-Luminosity LHC operation.

4.2 Coil cooling

Following the choice of the iron core magnets, and consequently the very low electrical power needed in the order of 1.5 kW for both MSM and HCM, air cooling has been adopted for the coil. Further margin is also given by the very large heat exchange surfaces. With respect to the underground location of the detector, this clearly brings significant advantages in terms of reduced complexity and increased reliability, compared to the relatively small penalty in terms of slightly larger coil sizes. The choice of a current density of 0.75 A/mm^2, which is less than the typical values considered for air-cooled normal-conducting magnets, i.e. 1 A/mm^2 [17, 27], guarantees that natural convection is sufficient to keep the temperature of the magnet low enough to avoid overheating of any sensitive part, in particular of the resin. A detailed thermal analysis of the designed system is out of the scope of this paper and should be considered for the following design phases.

4.3 Magnet assembly aspects

The mechanical design of the magnet system is partly driven by the constraints arising from the planned location in the TI18 tunnel, that is, limitations related to the access to TI18 and limitations on the handling of large and heavy pieces within the tunnel. Size and weight need to be considered in the design of each piece. As a result, the magnet system is planned to be transported and assembled in situ from segments.

With presently known constraints, and in particular the foreseen payload of the crane in the experimental area of 1.2 tonnes, a certain hypothesis of segmentation is given for the iron magnetic structure and the coils.

For the HCM, even in case of single iron yoke slabs of 8 cm thickness, the resulting mass is of 1.02 tonnes, well within the limits of the crane load capacity. Moreover, in order to install the coil, each slab has necessarily to be divided into two parts, as shown in figure 20.

For the MSM, the yoke is longitudinally split into 32 slabs, each one 5 cm thick. Also in this case, the iron slabs are divided in two parts each of the same shape as for the HCM. In this way, the maximum weight never exceeds 1.0 tonnes, again meeting the crane load capacity.

The final considerations concern the coils, which in total correspond to 1.3 tonnes (HCM) and 1.25 tonnes (MSM), respectively, i.e. slightly above the crane load capacity. However, they may both be divided in two coils, electrically connected in series, without major impact from the design point of view. Alternatively, one can consider the aluminium solution for the coil, at the price of a larger coil height. This solution has been discarded up to now in order to limit the overall size.

4.4 Cost estimate

A preliminary cost estimate has been prepared for the HCM and the MSM spectrometer magnets of the upgraded SND@LHC detector, following the standard approach given in reference [28], and used as well in reference [10]. It has to be emphasised that the choice of the core filled with iron,

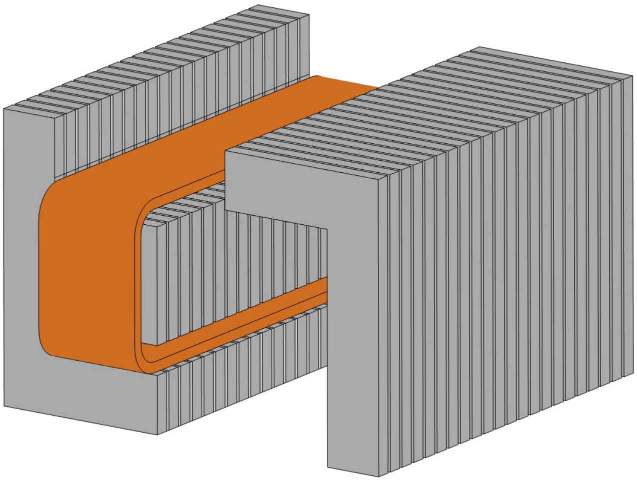

Figure 20. Segmentation of HCM with an upside-down F-L structure.

with the corresponding electrical power in the order of 1–2 kW, results in a negligible operational cost related to power. Consequently, only capital costs are considered.

The supply cost is evaluated based on present day pricing of raw materials, with specific (standard) manufacturing factors applied that are typically different for iron (magnetic structure) and copper (coil) and are assumed to account for possible manufacturing operations required to satisfy the design needs. The cost of the power converters is not yet finalized, as it may sensibly vary depending on the expected radiation levels in the TI18 tunnel that, as stated, are currently being evaluated [24–26] and extrapolated to High-Luminosity LHC operation. An extra cost, at the moment difficult to evaluate, is due to the local transport of the magnet system parts from surface to the TI18 tunnel, and the in situ assembly.

The estimated costs for the spectrometer system magnets are summarised in table 3. Costs related to cabling and piping (AC and DC power lines, cooling-water and control bus (worldfip)) are also not included in the estimate.

Table 3. Cost estimates in kCHF for the magnets of the spectrometer system.

	Unit cost	Units	Manufacturing factor	Cost
Hadron Calorimeter Magnet				
Coil (copper)	7.4/t	1.3 t	3	29
Magnetic structure (iron)	1.6/t	22.5 t	4	144
Muon System Magnet				
Coil (copper)	7.4/t	1.25 t	3	28
Magnetic structure (iron)	1.6/t	33 t	4	211
Total				412

5 Conclusions

This paper reports on the design of the magnetic spectrometer system for the upgrade of the SND@LHC experiment. It demonstrates that the proposed design with iron-core flux-symmetric magnets is an

2024 JINST 19 P12002

efficient solution, fully compliant with the physics requirements and the constraints from logistics. The problems of minimising the overall magnet size, low power, simplified coil (air) cooling and design robustness versus uncertainties of the iron quality and heats, have been tackled with detailed modeling, identifying a viable optimal set of design parameters. Accurate 3-D FEM electromagnetic simulations have been carried out to validate the design, providing the magnetic field maps in the active regions and the stray fields outside of the magnetic system. The design incorporates segmentation to respect the limitations on the transport and assembly procedures at the underground location. In total the magnet system is expected to cost below 0.5 MCHF.

Acknowledgments

We acknowledge the support provided by the following funding agencies: CERN; the Bulgarian Ministry of Education and Science within the NationalRoadmap for Research Infrastructures 2020–2027 (object CERN); ANID — Millennium Program — ICN2019_044 (Chile); FONDECYT (Chile) Grants No. 1240066, No. 1240216, No. 3230806; the Deutsche Forschungsgemeinschaft (DFG, ID 496466340); the Italian National Institute for Nuclear Physics (INFN); JSPS, MEXT, the Global COE program of Nagoya University, the Promotion and Mutual Aid Corporation for Private Schools of Japan for Japan; the National Research Foundation of Korea with grant numbers 2021R1A2C2011003, 2020R1A2C1099546, 2021R1F1A1061717, and 2022R1A2C100505; Fundação para a Ciência e a Tecnologia, FCT (Portugal), CERN/FIS-INS/0028/2021; the Swiss National Science Foundation (SNSF); TENMAK for Turkey (Grant No. 2022TENMAK (CERN) A5.H3.F2-1). The work of Valentino Scalera is funded by the European Union program FSE-REACT-EU, Pon Ricerca e Innovazione 2014–2020, DM 1062/2021, under the contract 41-I-15372-2 CUP: I65F21001200001. M. Climescu, H. Lacker and R. Wanke are funded by the Deutsche Forschungsgemeinschaft (DFG, German Research Foundation), Project 496466340. We acknowledge the funding of individuals by Fundação para a Ciência e a Tecnologia, FCT (Portugal) with grant numbers CEECIND/01334/2018, CEECINST/00032/2021 and PRT/BD/153351/2021. This research was financially supported under the National Recovery and Resilience Plan (NRRP), Mission 4, Component 2, Investment 1.1, Call for tender No. 104 published on 2.2.2022 by the Italian Ministry of University and Research (MUR), funded by the European Union — NextGenerationEU — Project Title: New physics, fundamental engineering and technological challenges in the emerging era of neutrino detectors at the Large Hadron Collider: feasibility study in view of an upgrade of the SND@LHC experiment for the high- luminosity LHC — CUP E53D2300228 0006 — Grant Assignment Decree No. 974 adopted on 30/06/2023 by the Italian Ministry of University and Research (MUR).

References

[1] SND@LHC collaboration, *SND@LHC: the scattering and neutrino detector at the LHC*, 2024 *JINST* **19** P05067 [`arXiv:2210.02784`].

[2] D. Abbaneo et al., *AdvSND, The Advanced Scattering and NeutrinoDetector at High Lumi LHC Letter of Intent*, CERN-LHCC-2024-007 (2024).

[3] ATLAS collaboration, *Luminosity determination in pp collisions at* $\sqrt{s} = 8$ *TeV using the ATLAS detector at the LHC*, *Eur. Phys. J. C* **76** (2016) 653 [`arXiv:1608.03953`].

[4] S. Buontempo, G.M. Dallavalle, G. De Lellis, D. Lazic and F.L. Navarria, *CMS-XSEN: LHC Neutrinos at CMS. Experiment Feasibility Study*, CERN-CMS-NOTE-2018-001 [`arXiv:1804.04413`].

[5] M. Buzio, *Technical and physiological hazards of static magnetic fields*, talk given at the *Seminar on Non-Ionising Radiation*, CERN, Geneva, 14 May 2019, https://indico.cern.ch/event/813103/.

[6] CERN, *GSI-NIR-1 — Protection of persons from Exposure to Static Magnetic Fields*, CERN, Geneva, Switzerland (2024), https://www.cern.ch/safety-rules.

[7] A. Quercia and V.P. Loschiavo, *Compact flux-symmetric conical magnets*, in preparation.

[8] CERN, *LHC Long term plan*, https://lhc-commissioning.web.cern.ch/schedule/LHC-long-term.htm.

[9] V. Scalera, *Analytical tools for the evaluation of the AvdSND FAR magnetic spectrometer performance*, SNDLHC-NOTE-2024-001.

[10] SHiP collaboration, *The magnet of the scattering and neutrino detector for the SHiP experiment at CERN*, 2020 *JINST* **15** P01027 [`arXiv:1910.02952`].

[11] American Iron and Steel Institute (AISI), https://www.steel.org.

[12] AK Steel ARMCO Pure Iron, https://www.aksteel.eu/products/armco-pure-iron/.

[13] S. Sgobba, *Physics and measurements of magnetic materials*, in the proceedings of the *CAS — CERN Accelerator School: Specialised course on Magnets*, Bruges, Belgium, 16–25 June 2009, CERN, Geneva, Switzerland (2010), pp. 39–63 [CERN-2010-004] [`arXiv:1103.1069`].

[14] ATLAS experiment, https://atlas.cern.

[15] M. Ambrosio et al., *The OPERA magnetic spectrometer*, *IEEE Trans. Nucl. Sci.* **51** (2004) 975 [`physics/0409137`].

[16] A. Cazes et al., *Electromagnetic characterization of the* 990 *ton gapless magnets for the OPERA experiment*, 2007 *JINST* **2** T03001.

[17] T. Zickler, *Basic design and engineering of normal-conducting, iron-dominated electromagnets*, in the proceedings of the *CERN Accelerator School: Course on Magnets*, Bruges, Belgium, 16–25 June 2009, `arXiv:1103.1119`.

[18] G.E. Fischer, *Iron dominated magnets*, *AIP Conf. Proc.* **153** (1987) 1120.

[19] M.A. Green, *Use of Aluminum Coils Instead of Copper Coils in Accelerator Magnet Systems*, *IEEE Trans. Nucl. Sci.* **14** (1967) 398.

[20] P.P. Silvester and R.L. Ferrari, *Finite Elements for Electrical Engineers*, third edition, Cambridge University Press, Cambridge, U.K. (1996) [`DOI:10.1017/cbo9781139170611`].

[21] J.P.A. Bastos and N. Sadowski, *Magnetic materials and* 3*D finite element modeling*, *MRS Bull.* **40** (2015) 184.

[22] COMSOL, *COMSOL Multiphysics®*, version 6.1 (2022), https://www.comsol.com/release/6.1.

[23] P. Odier, M. Ludwig and S. Thoulet, *The DCCT for the LHC beam intensity measurement*, in the proceedings of the *Beam Diagnostics and Instrumentation for Particle Accelerators*, Basel, Switzerland, 25–27 May 2009, CERN-BE-2009-019.

[24] A. Zimmaro et al., *Testing and Validation Methodology for a Radiation Monitoring System for Electronics in Particle Accelerators*, *IEEE Trans. Nucl. Sci.* **69** (2022) 1642.

[25] A. Zimmaro, S. Danzeca and S. Fiore, *Report on the 2023 BatMon measurements at the LHC and SPS*, talk given at the *57th MCWG meeting*, CERN, Geneva, 12 December 2023.

[26] A. Zimmaro, S. Danzeca and S. Fiore, *Report on the radiation on electronics measurements for SND@LHC experiment in TI18 Gallery, LHC-P1 Side*, EDMS #3029778, CERN, Geneva, Switzerland, 13 February 2024.

[27] S. Myers and H. Schopper, *Particle Physics Reference Library. Volume 3: Accelerators and Colliders*, Springer, Cham, Switzerland (2020) [ISBN: 978-3-030-34244-9] [`DOI:10.1007/978-3-030-34245-6`].

[28] M.A. Green, S.S. Chouhan and A.F. Zeller, *Cost Optimization of MSU Conventional Room Temperature Magnets as a Function of Magnet Conductor Current Density*, *IEEE Trans. Appl. Supercond.* **22** (2012) 4002504.

The SND@LHC collaboration

D. Abbaneo[i], S. Ahmad[am], R. Albanese[a,b], A. Alexandrov[a], F. Alicante[a,b], K. Androsov[f], A. Anokhina[c], T. Asada[a,b], C. Asawatangtrakuldee[ai], M.A. Ayala Torres[ad], C. Battilana[d,e], A. Bay[f], A. Bertocco[a,b], C. Betancourt[g], D. Bick[h], R. Biswas[i], A. Blanco Castro[j], V. Boccia[a,b], M. Bogomilov[k], D. Bonacorsi[d,e], W.M. Bonivento[l], P. Bordalo[j], A. Boyarsky[m,n], S. Buontempo[a], M. Campanelli[o], T. Camporesi[i], V. Canale[a,b], A. Castro[d,e], D. Centanni[a,p], F. Cerutti[i], M. Chernyavskiy[c], K.-Y. Choi[q], S. Cholak[f], F. Cindolo[d], M. Climescu[r], A.P. Conaboy[s], G.M. Dallavalle[d], D. Davino[a,t], P.T. de Bryas[f], G. De Lellis[a,b], M. De Magistris[a,p], A. De Roeck[i], A. De Rújula[i], D. De Simone[g], A. Di Crescenzo[a,b], D. Di Ferdinando[d], C. Dinc[u], R. Donà[d,e], O. Durhan[u], F. Fabbri[d], F. Fedotovs[o], M. Ferrillo[g], A. Fiorillo[a,b], R. Fresa[a,v], W. Funk[i], F.M. Garay Walls[w], A. Golovatiuk[a,b], A. Golutvin[x], E. Graverini[f,al], A.M. Guler[u], V. Guliaeva[c], G.J. Haefeli[f], C. Hagner[h], J.C. Helo Herrera[y,ak], E. van Herwijnen[x], P. Iengo[a], S. Ilieva[a,b,k], A. Infantino[i], A. Iuliano[a,b], R. Jacobsson[i], C. Kamiscioglu[u,z], A.M. Kauniskangas[f], E. Khalikov[c], S.H. Kim[aa], Y.G. Kim[ab], G. Klioutchnikov[i], M. Komatsu[ac], N. Konovalova[c], S. Kuleshov[y,ad], L.Krzempek[a,b,i], H.M. Lacker[s], O. Lantwin[a], F. Lasagni Manghi[d], A. Lauria[a,b], K.Y. Lee[aa], K.S. Lee[ae], S. Lo Meo[d], V.P. Loschiavo[a,t,*], S. Marcellini[d], A. Margiotta[d,e], A. Mascellani[f], F. Mei[e], A. Miano[a,b], A. Mikulenko[m], M.C. Montesi[a,b], F.L. Navarria[d,e], W. Nuntiyakul[aj], S. Ogawa[af], N. Okateva[c], M. Ovchynnikov[m], G. Paggi[d,e], B.D. Park[aa], A. Perrotta[d], D. Podgrudkov[c], N. Polukhina[c], A. Prota[a,b], A. Quercia[a,b,*], S. Ramos[j], A. Reghunath[s], T. Roganova[c], F. Ronchetti[f], T. Rovelli[d,e], O. Ruchayskiy[ag], T. Ruf[i], M. Sabate Gilarte[i], Z. Sadykov[a], M. Samoilov[c], V. Scalera[a,p,*], W. Schmidt-Parzefall[h], O. Schneider[f], G. Sekhniaidze[a], N. Serra[g], M. Shaposhnikov[f], V. Shevchenko[c], T. Shchedrina[c], L. Shchutska[f], H. Shibuya[af,1], G.P. Siroli[d,e], G. Sirri[d], G. Soares[j], J.Y. Sohn[aa], O.J. Soto Sandoval[y,ak], M. Spurio[d,e], N. Starkov[c], J. Steggemann[f], I. Timiryasov[ag], V. Tioukov[a], C. Trippl[f], E. Ursov[c], A. Ustyuzhanin[a,ah], G. Vankova-Kirilova[k], G. Vasquez[g], V. Verguilov[k], N. Viegas Guerreiro Leonardo[j], C. Vilela[j], C. Visone[a,b], R. Wanke[r], E. Yaman[u], Z. Yang[f], C. Yazici[u], C.S. Yoon[aa], E. Zaffaroni[f], J. Zamora Saa[y,ad]

[a] *Sezione INFN di Napoli, Napoli 80126, Italy*
[b] *Università di Napoli "Federico II", Napoli 80126, Italy*
[c] *Affiliated with an institute covered by a cooperation agreement with CERN*
[d] *Sezione INFN di Bologna, Bologna 40127, Italy*
[e] *Università di Bologna, Bologna 40127, Italy*
[f] *Institute of Physics, EPFL, Lausanne 1015, Switzerland*
[g] *Physik-Institut, UZH, Zürich 8057, Switzerland*
[h] *Hamburg University, Hamburg 22761, Germany*
[i] *European Organization for Nuclear Research (CERN), Geneva 1211, Switzerland*
[j] *Laboratory of Instrumentation and Experimental Particle Physics (LIP), Lisbon 1649-003, Portugal*
[k] *Faculty of Physics, Sofia University, Sofia 1164, Bulgaria*
[l] *Università degli Studi di Cagliari, Cagliari 09124, Italy*
[m] *University of Leiden, Leiden 2300RA, The Netherlands*
[n] *Taras Shevchenko National University of Kyiv, Kyiv 01033, Ukraine*
[o] *University College London, London WC1E6BT, United Kingdom*
[p] *Università di Napoli "Parthenope", Napoli 80143, Italy*
[q] *Sungkyunkwan University, Suwon-si 16419, Korea*
[r] *Institut für Physik and PRISMA Cluster of Excellence, Mainz 55099, Germany*

2024 JINST 19 P12002

[s] Humboldt-Universität zu Berlin, Berlin 12489, Germany
[t] Università del Sannio, Benevento 82100, Italy
[u] Middle East Technical University (METU), Ankara 06800, Turkey
[v] Università della Basilicata, Potenza 85100, Italy
[w] Departamento de Física, Pontificia Universidad Católica de Chile, Santiago 4860, Chile
[x] Imperial College London, London SW72AZ, United Kingdom
[y] Millennium Institute for Subatomic Physics at High Energy Frontier, SAPHIR, Santiago 7591538, Chile
[z] Ankara University, Ankara 06100, Turkey
[aa] Department of Physics Education and RINS, Gyeongsang National University, Jinju 52828, Korea
[ab] Gwangju National University of Education, Gwangju 61204, Korea
[ac] Nagoya University, Nagoya 464-8602, Japan
[ad] Center for Theoretical and Experimental Particle Physics, Facultad de Ciencias Exactas, Universidad Andrès Bello, Fernandez Concha 700, Santiago, Chile
[ae] Korea University, Seoul 02841, Korea
[af] Toho University, Chiba 274-8510, Japan
[ag] Niels Bohr Institute, Copenhagen 2100, Denmark
[ah] Constructor University, Bremen 28759, Germany
[ai] Chulalongkorn University, Bangkok 10330, Thailand
[aj] Chiang Mai University , Chiang Mai 50200, Thailand
[ak] Departamento de Física, Facultad de Ciencias, Universidad de La Serena, La Serena 1200, Chile
[al] Università di Pisa, Pisa 56126, Italy
[am] Pakistan Institute of Nuclear Science and Technology (PINSTECH), Nilore 45650, Islamabad, Pakistan

[*] Corresponding author
[1] Now at: Faculty of Engineering, Kanagawa 221-0802, Japan

2024 JINST 19 P12002